DUAL SATELLITE-AIDED PLANETARY CAPTURE WITH INTERPLANETARY TRAJECTORY CONSTRAINTS

Christopher J. Scott(1), Martin T. Ozimek(2), Amanda F. Haapala(3), Brent B. Buffington(4), and Fazle E. Siddique(5)
(1)Johns Hopkins University Applied Physics Laboratory, 11100 Johns Hopkins Rd. Laurel, Maryland, 20723, (240) 228-5120, Christopher.Scott@jhuapl.edu
(2)Johns Hopkins University Applied Physics Laboratory, 11100 Johns Hopkins Rd. Laurel, Maryland, 20723, (240) 228-1569, Martin.Ozimek@jhuapl.edu
(3)Johns Hopkins University Applied Physics Laboratory, 11100 Johns Hopkins Rd. Laurel, Maryland, 20723, (240) 228-2382, Amanda.Haapala@jhuapl.edu
(4)Jet Propulsion Laboratory, 4800 Oak Grove Drive Pasadena, California, 91109, (818) 393-7964, Brent.B.Buffington@jpl.nasa.gov
(5)Johns Hopkins University Applied Physics Laboratory, 11100 Johns Hopkins Rd. Laurel, Maryland, 20723, (240) 228-9270, Fazle.Siddique@jhuapl.edu

Abstract: *The system entry problem entails the capture of a spacecraft about a planet by way of propulsive maneuver(s) or flyby(s) of a planetary satellite(s), or both. In the case of the Jovian system, a balance is sought between the interplanetary time-of-flight, orbit insertion maneuver magnitude, mass delivered to the system, capture orbit period, radiation dose, and mission complexity. Based on a nominal asymptote, this paper introduces the analytical equations necessary to solve the phase-free, singly-aided and doubly-aided capture problems, with a focus on the doubly-aided capture problem in the Jovian system. An analytical approximation for the required phasing is derived and the implications of the Laplace resonance are discussed. Analytical approximations are used to seamlessly seed a multiple-shooting algorithm in order to arrive at the converged high-fidelity solution space for the Europa Mission.*

Keywords: *Mission Design, Trajectory Design, System Entry, Capture, Singly Aided, Doubly Aided, Moon, Jupiter, Io, Europa, Callisto, Ganymede.*

1. Introduction

Gravity assist aided capture into a planetary system can significantly reduce the propulsive requirements of an insertion maneuver, and for a given launch vehicle, increase the delivered dry mass that can be utilized for scientific instrumentation or other spacecraft subsystems, and/or potentially allowing a shorter time-of-flight interplanetary trajectory to the planetary system. The only example of aided capture to date is the Galileo mission, which performed an Io assisted capture in 1995, reducing the insertion maneuver by about 175 m/s. Interestingly, it had an untargeted Europa encounter of 32,000 km altitude, 4.6 hours prior to the Io flyby.[1] The trajectory likely came close to a doubly-aided solution.

As early as the 1960's, Longman [2, 3] studied each moon's ability to affect capture about Jupiter in terms of energy, yet he did not determine the specifics of the actual trajectories. The possible energy change available from two-moon encounter combinations was additionally quantified. Cline [4] studied the possibility of a single flyby capture within the solar system and concluded that it is not possible to capture without a maneuver assuming a direct Earth launch, excluding a possible Triton assisted capture. Nock [5] studied phase-free, singly-aided assisted captures in many systems with finite declinations, including powered flybys. Over the past several years, Lynam has published many works on the topic investigating both double- and triple-flyby sequences by deriving the relative phasing constraints and the associated directions of the incoming Jupiter excess velocities.[6, 7, 8] Feasible interplanetary trajectory candidates, limited to direct interplanetary trajectories, were identified by backwards propagation.

The proposed solution process differs from previous work in that a prediction for the doubly-aided sequence is derived assuming a fixed interplanetary arrival asymptote. This assumption is due to the fact that an enabling interplanetary trajectory, without regard to satellite-aided capture, accounts for the majority of the total energy (Δv and delivered mass) and time-of-flight requirements. The interplanetary trajectory may also define thermal requirements on the spacecraft from the extremes in solar distance, as well as communication gaps to the Earth due to solar conjunctions. Thus, the pragmatic mission design work-flow initiates with an exhaustive global interplanetary search, taking into account the aforementioned system-driving considerations prior to selection. Within this work-flow, single and double satellite-aided system capture is treated as an enhancement option to further improve a given interplanetary design. Thus, the approach presented here is a forwards method in that only small timing adjustments are introduced to an interplanetary trajectory of interest to produce a potential doubly-aided capture scenario. The process also reduces the design space to a small region of interest by automatically omitting the infeasible solution space. Finally, this approach is applicable to any interplanetary solution, such as direct trajectories or multi-gravity assists (e.g. VEEGA's). A seamless process to convert an analytical prediction to an end-to-end, Earth to Jupiter orbit insertion (JOI) optimized, high-fidelity trajectory is introduced. A detailed derivation and description of the doubly-aided combinations that open the design space to finite incoming declinations is additionally demonstrated.

Currently, the Europa Project has a baseline design that utilizes a single 300 km Ganymede flyby prior to the JOI maneuver, resulting in a 200-day period capture orbit. There is an ongoing trade study to understand potential propellant mass savings and system impact from a double capture scenario. Doubly-aided solutions provide access to a flight time of the subsequent tour versus Δv savings trade space at the expense of increased mission complexity (navigation and spacecraft design). An extreme example is to insert into the nominal 200-day orbit while realizing the maximum Δv savings of the doubly-aided solution. Alternatively, it is possible to capture into a lower period orbit, trading reduced flight time for Δv.

2. Solution Process

Using the methods detailed in this paper, Fig. 1 shows the capture contours of all ballistic dual satellite flyby solutions in the Jupiter system as a function of incoming system hyperbolic excess velocity and satellite flyby altitude. For simplicity, both flyby altitudes are held to the same value of 500 km and the incoming hyperbola is in the plane of the moons. Here, capture is defined as zero Jupiter two-body energy at the end of the dual-flyby sequence, and solutions below the curves represent all entry conditions resulting in ballistic capture. Under the assumptions of co-planar, circular planetary orbits, a minimum arrival v_∞ of 5.65 km/s for a direct Earth-to-Jupiter Hohmann transfer would not result in a captured solution from a purely ballistic dual flyby system entry. Therefore, all solutions investigated in this paper involve a propulsive maneuver near Jupiter.

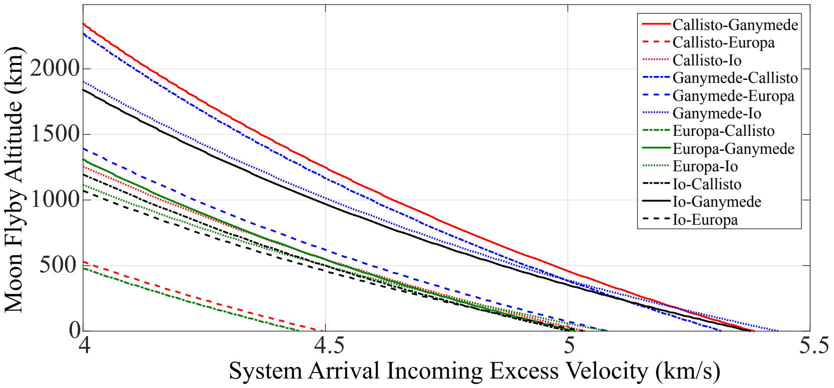

Figure 1: Dual flyby ballistic capture contours

Efforts to develop the analytical, phase-free approximation stem from a desire to rapidly identify enabling trajectories and assess associated Δv cost/savings. The flyby-maneuver-flyby (FMF) sequence is the most likely for a non-zero excess velocity declination.[1] The major drawback of this sequence is that the uncertainty of the spacecraft state is amplified by the large maneuver before the second flyby. It is for this reason that maneuver-flyby-flyby sequences are not considered. In the flyby-flyby-maneuver (FFM) sequence, the first flyby must eliminate the inclination with respect the orbital plane of the moons or the interplanetary trajectory must be modified such that the incoming asymptote has zero declination. In this study, the FFM sequences are produced by constraining the interplanetary asymptote to have zero declination with respect to the moon plane since reasonable changes in the DSM magnitude are realized.

A search for doubly-aided sequences begins by considering the phase-free problem, where the phasing of the moons is not yet incorporated. An analytical solution is derived, with key assumptions for the phase-free approximation are listed as follows:

1. The orbits of the moons are circular and coplanar.
2. An impulsive maneuver is applied at the planetary periapsis.
3. The maneuver is in the anti-velocity direction.
4. Zero sphere-of-influence (ZSOI) flybys are modeled.
5. The flybys minimize energy with respect to the central body.
6. The inbound asymptote into the system is fixed.

A simple phasing check using planetary and moon ephemerides is used to match candidate phase-free trajectories with nominal arrival dates. Once a candidate trajectory is matched with an arrival date, it is transitioned to a high-fidelity model using simplified models for the planetary and satellite ephemerides. For the purpose of this study, the JPL in-house high-fidelity optimization software, Computer Optimization System for Multiple Independent Courses (COSMIC), is used to reconverge the solution within the ephemeris model. The doubly-aided sequences are numerically sensitive by nature. Therefore, an intermediate refinement step is necessary to lift the assumption of circular

---

[1] with respect to the orbital plane of the planetary satellites

orbits during the transition to the ephemeris model. This refinement step entails a simple nonlinear programming algorithm which uses the ephemerides to refine the solution. The refinement helps to place the approximation within the basin of convergence of the optimization algorithm. The solution process is summarized in Fig. 2.

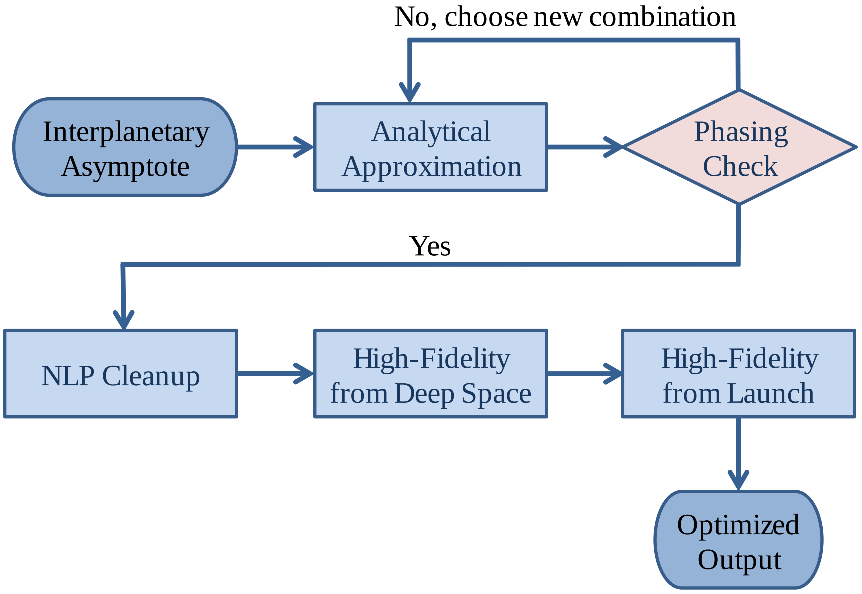

Figure 2: Solution process

3. Analytical Predictions

In the following sections, a detailed derivation of the states defining segments along doubly-aided sequences is demonstrated. The assumptions listed in section 2 are applied to both the FMF and FFM cases.

3.1. Flyby-Maneuver-Flyby Sequences

The phase-free doubly-aided solution for the FMF sequence is analytically calculated in five steps with a sixth step to estimate the phasing. These steps are outlined as follows:

1. Select a value, r_p, for the perijove radius of the incoming hyperbola.
2. Calculate the orbital elements of the incoming hyperbola, subject to the constraints on the incoming asymptote and constraining the radius of the first node to be equal to the orbit radius of the first flyby body.
3. Based on the B-plane target of the first flyby body that minimizes energy relative to Jupiter, calculate the orbital elements after the first flyby.
4. Find the orbital elements after the maneuver subject to the second node radius, perijove radius, and maneuver direction constraints.
5. Based on the B-plane target of the second flyby body that minimizes energy relative to Jupiter, calculate the orbital elements after the second flyby.
6. Calculate the time-of-flight of each segment to provide a relative (angle subtended between flybys) and absolute (angle orienting the first flyby relative to an inertial frame) phasing guess.

The orbital elements before and after the first flyby, after the maneuver at perijove, and after the second flyby are defined analytically from the imposed constraints, as previously described. Expressions for these elements are derived in the following sections.

3.1.1. Orbital elements of the incoming hyperbola

The orbital elements of the incoming hyperbola are prescribed by the incoming asymptote and radius of the first node. All orbital elements in the expressions within this section correspond to the incoming hyperbola before the flyby, and are relative to the central body. The inertial excess velocity with respect to the central body is expressed as

$$\mathbf{v}_\infty^- = v_\infty \left[\begin{array}{ccc} \cos\alpha_e \cos\delta_e & \sin\alpha_e \cos\delta_e & \sin\delta_e \end{array} \right]^T \tag{1}$$

where α_e and δ_e are the right ascension and declination of the incoming asymptote with respect to the planet. If the x-y plane of the inertial frame lies in the orbital plane of the planetary satellite, then the range of possible inclinations of the incoming hyperbola with respect to this plane is $\delta_e \leq i \leq \pi - \delta_e$.

For a finite declination, the radius of the ascending or descending node of the hyperbola must equal that of the planetary satellite for a flyby to be possible under the ZSOI assumption. Using the orbit equation, the true anomaly at a node is

$$\theta_{N1} = \left\{ \begin{array}{cc} \arccos\left(\frac{p}{eR_{N1}} - \frac{1}{e}\right) & \text{(flyby after periapsis)} \\ -\arccos\left(\frac{p}{eR_{N1}} - \frac{1}{e}\right) & \text{(flyby before periapsis)} \end{array} \right\} \tag{2}$$

where R_{N1} is the radius of the node, p is the semi-parameter, and e is the eccentricity about the central body. The argument of periapsis is

$$\omega = \left\{ \begin{array}{cc} -\theta_{N1} & \text{(flyby at ascending node)} \\ \pi - \theta_{N1} & \text{(flyby at descending node)} \end{array} \right\} \tag{3}$$

and the radius at the node is

$$R_{N1} = \left\{ \begin{array}{cc} \frac{p}{1+e\cos(-\omega)} & \text{(flyby at ascending node)} \\ \frac{p}{1+e\cos(\pi-\omega)} & \text{(flyby at descending node)} \end{array} \right\} \tag{4}$$

Because $R_{N1} > 0$, the existence of the nodes is given as follows:

$$\begin{array}{c} \cos\omega > -\frac{1}{e} : \text{ascending node exists} \\ \cos\omega < \frac{1}{e} : \text{descending node exists} \\ -\frac{1}{e} < \cos\omega < \frac{1}{e} : \text{both ascending and descending nodes exist} \end{array} \tag{5}$$

The incoming asymptote is connected to the orbital elements of the hyperbola using the standard perifocal frame, $\hat{\mathbf{p}}$-$\hat{\mathbf{q}}$-$\hat{\mathbf{w}}$, as

$$\mathbf{v}_\infty^{pqw-} = P\mathbf{v}_\infty^- \tag{6}$$

where the elements P_{ij} of P are given as

$$\begin{aligned}
P_{11} &= \cos\Omega\cos\omega - \sin\Omega\sin\omega\cos i \\
P_{12} &= \sin\Omega\cos\omega + \cos\Omega\sin\omega\cos i \\
P_{13} &= \sin\omega\sin i \\
P_{21} &= -\cos\Omega\sin\omega - \sin\Omega\cos\omega\cos i \\
P_{22} &= -\sin\Omega\sin\omega + \cos\Omega\cos\omega\cos i \\
P_{23} &= \cos\omega\sin i \\
P_{31} &= \sin\Omega\sin i \\
P_{32} &= -\cos\Omega\sin i \\
P_{33} &= \cos i
\end{aligned} \tag{7}$$

Here, Ω and i are the right ascension of the ascending node and inclination with respect to the central body, respectively. The velocity $\mathbf{v}_{\infty}^{pqw-}$ is obtained via the true anomaly at negative infinity, θ_{∞}, yielding the approach velocity of the hyperbolic orbit:

$$\mathbf{v}_{\infty}^{pqw-} = \left[\begin{array}{ccc} v_{\infty x}^{pqw} & v_{\infty y}^{pqw} & 0 \end{array}\right] = \sqrt{\frac{\mu_c}{p}} \left[\begin{array}{ccc} \sin\theta_{\infty} & e+\cos\theta_{\infty} & 0 \end{array}\right]^T \tag{8}$$

where

$$\cos\theta_{\infty} = -\frac{1}{e} \tag{9}$$

Here, μ_c is the gravitational mass parameter of the central body. Note that the first two terms of $\mathbf{v}_{\infty}^{pqw-}$ are greater than zero in the $\hat{\mathbf{p}}$-$\hat{\mathbf{q}}$-$\hat{\mathbf{w}}$ frame. It follows that

$$\sin i = \frac{v_{\infty}\sin\delta_e}{v_{\infty y}^{pqw}\cos(\omega) + v_{\infty x}^{pqw}\sin(\omega)} = \frac{\sin\delta_e}{\cos\left(\omega + \arctan\left(-\frac{v_{\infty x}^{pqw}}{v_{\infty y}^{pqw}}\right)\right)} \tag{10}$$

where the quadrant is chosen in accordance with a prograde or retrograde solution. It also follows from Eq. 6 that

$$\Omega = \alpha_e - \arcsin\left(\frac{\tan(\delta_e)}{\tan(i)}\right) = \alpha_e + \arccos\left(\frac{v_{\infty x}^{pqw}\cos(\omega) - v_{\infty y}^{pqw}\sin(\omega)}{v_{\infty}\cos(\delta_e)}\right) \tag{11}$$

A quadrant check is performed by comparing the two expressions in equation 11.

The radius and velocity vectors at the node are now computed as

$$\begin{aligned}
\mathbf{r}_{N1} &= P^T \mathbf{r}_{N1}^{pqw} \\
\mathbf{v}_{N1}^{-} &= P^T \mathbf{v}_{N1}^{pqw-}
\end{aligned} \tag{12}$$

where

$$\begin{aligned}
\mathbf{r}_{N1}^{pqw} &= R_{N1} \left[\begin{array}{ccc} \cos\theta_{N1} & \sin\theta_{N1} & 0 \end{array}\right]^T \\
\mathbf{v}_{N1}^{pqw-} &= \sqrt{\frac{\mu_c}{p}} \left[\begin{array}{ccc} \sin\theta_{N1} & e+\cos\theta_{N1} & 0 \end{array}\right]^T
\end{aligned} \tag{13}$$

Thus, the full state at the node is defined analytically.

3.1.2. Orbital elements after the first flyby

The state associated with the hyperbola, relative to Jupiter, after the first flyby is defined, provided that the position of the flyby body at the first node is known. Assuming that the orbit of the planetary satellite is circular, its velocity at the flyby is

$$\mathbf{v}_{b1} = \sqrt{\frac{\mu_c}{R_{N1}}}\hat{\mathbf{v}}_1 \tag{14}$$

where $\hat{\mathbf{v}}_1$ is computed by identifying the direction, $\hat{\mathbf{r}}_1$, from the central body to the position of the planetary satellite, and the direction normal to the orbit, $\hat{\mathbf{h}}_1$. For a circular orbit,

$$\hat{\mathbf{v}}_1 = \frac{\hat{\mathbf{k}}_1 \times \hat{\mathbf{r}}_1}{||\hat{\mathbf{k}}_1 \times \hat{\mathbf{r}}_1||} \tag{15}$$

where

$$\begin{aligned} \hat{\mathbf{r}}_1 &= \tfrac{\mathbf{r}_{N1}}{||\mathbf{r}_{N1}||} \\ \hat{\mathbf{k}}_1 = \hat{\mathbf{h}}_1 &= \left[\begin{array}{ccc} 0 & 0 & 1 \end{array}\right]^T \end{aligned} \tag{16}$$

recalling that the *x*-*y* plane of the inertial frame is defined to lie within in the orbital plane of the flyby body. The incoming excess velocity relative to the planetary satellite is

$$\mathbf{v}_{\infty 1}^- = \mathbf{v}_{N1}^- - \mathbf{v}_{b1} \tag{17}$$

To determine the post-flyby velocity relative to Jupiter, consider the plane containing the incoming excess velocity and flyby body velocity vectors. The orientation of the outgoing excess velocity vector relative to this plane is defined using the angle β, depicted in Figure 16 in the appendix. A flyby that minimizes energy with respect to central body sets β to zero (see appendix for details). Then, the post-flyby velocity relative to the central body becomes

$$\mathbf{v}_{N1}^+ = \mathbf{v}_{b1} + \mathbf{v}_{\infty 1}^+ \tag{18}$$

with a post-flyby energy of E_{N1}^+. The orbital elements are, then, calculated from the state after the flyby.

3.1.3. Orbital elements after the maneuver

Assuming the spacecraft performs an impulsive maneuver at periapsis in the opposite direction of the velocity, the post-maneuver orbital elements relative to Jupiter are preserved except for the semi-major axis and eccentricity. The maneuver must place the next node at the radius, R_{N2}, of the second planetary satellite. Using the orbit equation, the semi-major axis after the maneuver is expressed as

$$a_{dv} = \frac{R_{N2} r_p \cos\theta_{N2} - r_p^2}{R_{N2} + R_{N2}\cos\theta_{N2} - 2r_p} \tag{19}$$

where the subscript (*dv*) indicates a condition after the maneuver at periapsis. It follows that

$$E_{dv} = -\frac{\mu_c}{2a_{dv}} \tag{20}$$

$$v_{p,dv} = \sqrt{2\left(E_{dv} + \frac{\mu_c}{r_p}\right)} \tag{21}$$

Note that the existence of a solution is not guaranteed for all cases, as Eq. 21 may result in an imaginary number. Differencing the energy before and after the maneuver gives the maneuver magnitude as

$$\Delta v = \frac{2\left(E_{dv} - E_{N1}^{+}\right)}{v_{p,dv} + v_p} \tag{22}$$

Any remaining orbital elements may additionally be computed via well-known astrodynamics relationships.

3.1.4. Calculating the orbital elements after the second flyby

After the maneuver, the spacecraft is propagated to the second node using Eq. 12. The velocity of the second planetary satellite is computed as before, and the incoming excess velocity is

$$\mathbf{v}_{\infty 2}^{-} = \mathbf{v}_{N2} - \mathbf{v}_{b2} \tag{23}$$

As in the previous case, β is set to zero to minimize energy, yielding the post-flyby velocity

$$\mathbf{v}_{N2}^{+} = \mathbf{v}_{b2} + \mathbf{v}_{\infty 2}^{+} \tag{24}$$

Again, the orbital elements associated with this segment are computed from the state at the second node.

3.2. Flyby-Flyby-Maneuver Sequences

The phase-free doubly-aided solution for the FFM sequence is analytically calculated in six steps. Because the maneuver occurs at perijove, the sequence requires the first encounter moon to be the outer moon, followed by the inner moon. The analytical process is outlined as:

1. Select a value for the perijove radius of the incoming hyperbola.
2. Calculate the orbital elements of the incoming hyperbola, subject to the constraints on the incoming asymptote and the radius of first flyby moon's orbit.
3. Based on a B-plane target that minimizes energy relative to Jupiter, calculate the orbital elements after the first flyby.
4. If the orbit resulting from the first flyby crosses the orbital radius of the second flyby moon, calculate the orbital elements after the second flyby based on a B-plane target that minimizes energy relative to Jupiter.
5. Calculate the maneuver value which results in the desired capture period.
6. Calculate the time-of-flight of each segment to provide a relative (angle subtended between flybys) and absolute (angle orienting the first flyby relative to an inertial frame) phasing guess.

3.2.1. Orientation of the incoming hyperbola

The major assumption associated with the FFM sequence is that the incoming declination relative to the orbital plane of the moons, δ_e, is zero. Then, the inertial excess velocity with respect to the central body becomes

$$\mathbf{v}_\infty^- = v_\infty \begin{bmatrix} \cos\alpha_e & \sin\alpha_e & 0 \end{bmatrix}^T \tag{25}$$

The incoming excess velocity written in the perifocal frame is

$$\mathbf{v}_\infty^{pqw-} = A\mathbf{v}_\infty^- = \sqrt{\frac{\mu_c}{p}} \begin{bmatrix} \sin\theta_\infty & e+\cos\theta_\infty & 0 \end{bmatrix}^T \tag{26}$$

where p and e are the semi-parameter and eccentricity of the incoming hyperbola, and

$$A = \begin{bmatrix} \cos\phi & \sin\phi & 0 \\ -\sin\phi & \cos\phi & 0 \\ 0 & 0 & 1 \end{bmatrix} \tag{27}$$

represents a rotation in the plane. It is straightforward to solve for the rotation angle ϕ and perform the associated quadrant check.

3.2.2. Orbital elements after the first and second flybys

Choosing the perijove radius, r_p, of the incoming hyperbola before the flyby and assuming that the flyby is performed prior to periapsis with respect to the central body, the true anomaly at the flyby along the incoming hyperbola is

$$\theta_{N1} = \arccos\left(\frac{p}{eR_1} - \frac{1}{e}\right) \tag{28}$$

where R_1 is the orbital radius of the first flyby moon. The excess velocity and velocity with respect to the central body before and after the flyby are computed in the same manner as the previous case with $\beta = 0$

$$\begin{aligned} \mathbf{r}_1 &= A^T \mathbf{r}_1^{pqw} \\ \mathbf{v}_1^- &= A^T \mathbf{v}_1^{pqw-} \end{aligned} \tag{29}$$

where $\mathbf{r}_1$ and $\mathbf{v}_1^-$ are the position and velocity of the spacecraft with respect to the central body before the flyby. Here, the state vector in the $\hat{\mathbf{p}}$-$\hat{\mathbf{q}}$-$\hat{\mathbf{w}}$-frame is given in Eq. 13 and

$$\mathbf{v}_{\infty 1}^- = \mathbf{v}_1^- - \mathbf{v}_{b1} \tag{30}$$

$$\mathbf{v}_1^+ = \mathbf{v}_{b1} + \mathbf{v}_{\infty 1}^+ \tag{31}$$

There is no guarantee that the trajectory will cross the radius of the second orbit for a given r_p; all infeasible solutions are discarded. For the feasible trajectory set, the velocity after the second flyby is calculated as

$$\mathbf{v}_{\infty 2}^- = \mathbf{v}_2^- - \mathbf{v}_{b2} \tag{32}$$

$$\mathbf{v}_2^+ = \mathbf{v}_{b2} + \mathbf{v}_{\infty 2}^+ \tag{33}$$

For a target period, T, the semi-major axis and energy after the maneuver are

$$\begin{aligned} a_{dv} &= \left(\tfrac{\mu_c T^2}{4\pi^2}\right)^{\frac{1}{3}} \\ E_{dv} &= -\tfrac{\mu_c}{2a_{dv}} \end{aligned} \tag{34}$$

If r_p is the radius of periapsis and v_p is the velocity of periapsis before the maneuver then,

$$\begin{aligned} v_{p,\text{targ}} &= \sqrt{2\left(E_{dv} + \frac{\mu_c}{r_p}\right)} \\ \Delta v &= v_{p,\text{targ}} - v_p \end{aligned} \tag{35}$$

3.3. Phasing

Once a given phase-free solution is located, the next step is to determine the available arrival epochs by locating times within the ephemerides that satisfy any phasing constraints. Pragmatically, an interplanetary trajectory is already selected for planetary arrival, as this segment of the trajectory typically has the most influence over minimization of total mission Δv. Given the typical time scales of planetary moon orbits compared to that of the interplanetary trajectory, it is reasonable to assume that the planetary arrival $\mathbf{v}_\infty^-$ vector is inertially fixed. This vector serves as a useful reference for determining which phase-free solutions meet the requirements of a phase-fixed solution. Assuming a planet-centered inertial reference frame where the $\hat{\mathbf{X}}$-$\hat{\mathbf{Y}}$ axes are constrained within the moon plane and the $\hat{\mathbf{Z}}$ axis is constrained with the north-pole vector, the *asymptote frame* $\hat{\mathbf{x}}^a$-$\hat{\mathbf{y}}^a$-$\hat{\mathbf{z}}^a$ may be constructed. Defining the $\hat{\mathbf{x}}^a$-axis as the projection of the asymptote into the moon plane, the frame is defined as

$$\hat{\mathbf{x}}^a = \frac{\begin{bmatrix} \mathbf{v}_\infty^- \cdot \hat{\mathbf{X}} & \mathbf{v}_\infty^- \cdot \hat{\mathbf{Y}} & 0 \end{bmatrix}^T}{\sqrt{(\mathbf{v}_\infty^- \cdot \hat{\mathbf{X}})^2 + (\mathbf{v}_\infty^- \cdot \hat{\mathbf{Y}})^2}} \tag{36}$$

$$\hat{\mathbf{y}}^a = \frac{\hat{\mathbf{Z}} \times \mathbf{x}^a}{||\hat{\mathbf{Z}} \times \mathbf{x}^a||} \tag{37}$$

$$\hat{\mathbf{z}}^a = \hat{\mathbf{x}}^a \times \hat{\mathbf{y}}^a \tag{38}$$

This asymptote frame is used as the basis for measuring angles for the phase-fixed problem.

For doubly-aided satellite capture, the phasing problem requires two angles to match at the epoch of the first flyby. Define θ_1 as the angle of the first encounter moon with respect to $\hat{\mathbf{x}}^a$ (i.e., the absolute phasing), and θ_r as the relative phasing angle between the two moons. Both angles are measured positive counter-clockwise, with desired values of $\theta_{1,\text{d}}$ and $\theta_{r,\text{d}}$ identified in the phase-free problem. A sketch of the moons in their desired configurations within the asymptote frame appears in Figure 3. In the phasing problem, it is assumed that a reference arrival epoch t_{ref}, consistent with the planetary arrival asymptote, is known. For this epoch, the moons are in arbitrary orientations with respect to the desired locations, as depicted in Figure 4(a). An encounter time, $t_1 = t_{\text{ref}} + \Delta t$, with the first moon is sought for which the required absolute phasing is available. It is desirable to minimize Δt in order to preserve the assumption that the arrival asymptote is inertially fixed. Sampling the moon ephemerides at t_{ref} yields $\theta_{1,0}(t_{\text{ref}})$ and $\theta_{r,0}(t_{\text{ref}})$, i.e., the initial absolute and relative phasing angles, respectively. The absolute angular velocities for the moons are n_1 and n_2, with relative angular velocity n_r. These angular rates are computed as

$$n_1 = 2\pi/T_1 \tag{39}$$

$$n_2 = 2\pi/T_2 \tag{40}$$

$$n_r = n_2 - n_1 \tag{41}$$

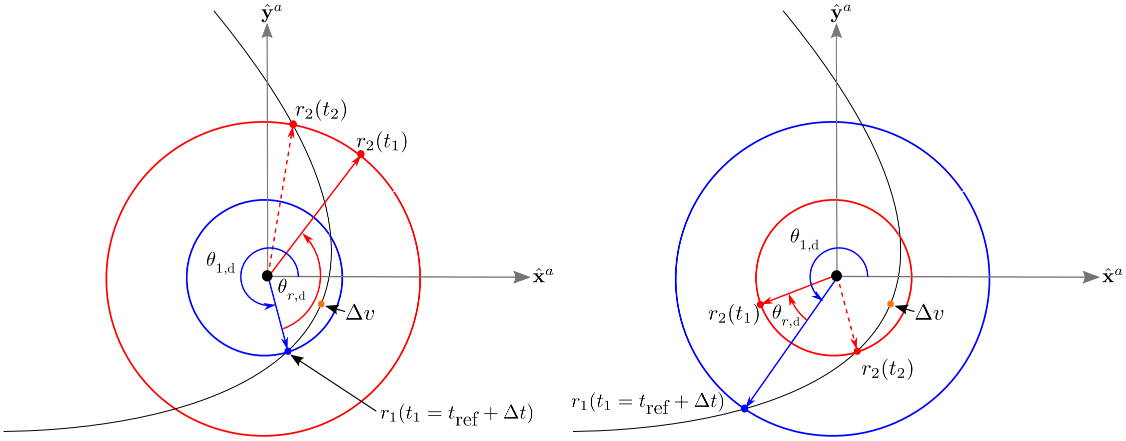

(a) FMF sequence

(b) FFM sequence

Figure 3: Desired moon configuration for a feasible doubly-aided capture sequence

where T_1 and T_2 are the orbital periods of the first and second bodies. The time history of the absolute and relative phasing is, then, simply

$$\theta_1 = \theta_{1,0}(t_{\mathrm{ref}}) + n_1 \Delta t \tag{42}$$

$$\theta_r = \theta_{r,0}(t_{\mathrm{ref}}) + n_r \Delta t \tag{43}$$

The most desirable solutions from the available phase-free set are those with a small maneuver at perijove and minimal Δt. Let the phasing time Δt be decomposed into two parts as

$$\Delta t = \Delta t_1 + \Delta t_{r,1} \tag{44}$$

The time until the desired relative phasing first occurs ($\theta_{r,1} = \theta_{r,\mathrm{d}}$) is

$$\Delta t_{r,1} = \frac{\theta_{r,\mathrm{d}} - \theta_{r,0}}{n_r} \tag{45}$$

with $\theta_1(t_{\mathrm{ref}} + \Delta t_{r,1}) = \theta_{1,1}$. This relative phasing repeats every $m \in \mathbb{Z}$ synodic periods

$$\theta_r = \theta_r + 2\pi m \tag{46}$$

where the synodic period T_s is

$$T_s = \frac{2\pi}{|n_r|} \tag{47}$$

With the relative phasing satisfied, the moons may still be in arbitrary orientations, as sketched in Figure 3. To satisfy both the relative phasing and the absolute phasing, it is required that,

$$\Delta t_1 = m T_s \tag{48}$$

so that the difference between the actual and desired phasing angles is

$$|\Delta\theta_1| = |\theta_{1,\mathrm{d}} - \theta_{1,1} - n_1 m T_s| < \varepsilon \tag{49}$$

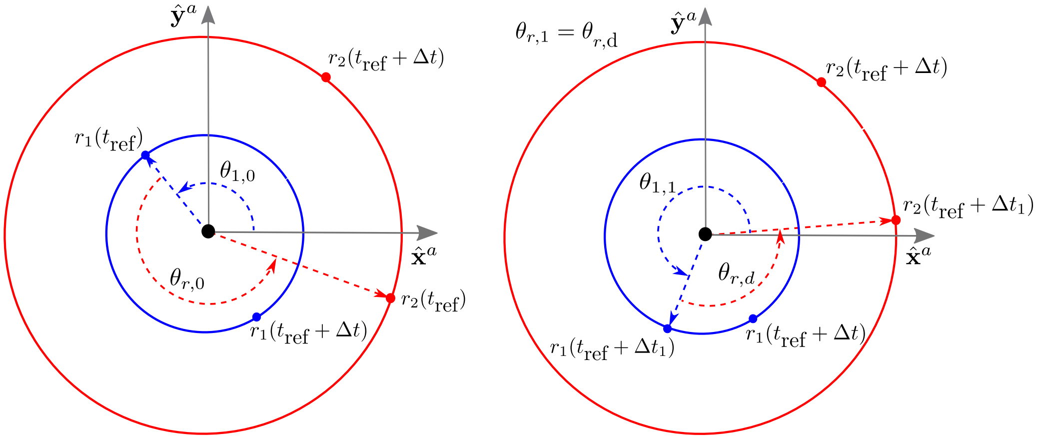

(a) At t_{ref}

(b) At $t_{\text{ref}} + \Delta t_{r,1}$

Figure 4: Moon orientations during solution process

where ε is a user-specified error tolerance. The tolerance ε is selected to minimize m while simultaneously maintaining a small discontinuity between the actual and desired phasing angles. The value of this tolerance is an important consideration when transitioning the analytical solution to a high-fidelity model. Considering both positive and negative values of m, values of $\varepsilon < 17^\circ$ are generally sufficient to locate a solution while maintaining $|\Delta t| < 40$ days to maintain predictions based on the nominal asymptote. Ideally, a balance between the magnitudes of ε and Δt can be found; otherwise, either ε or Δt is minimized while allowing an increase in the other. Locating an epoch that satisfies Eq. (49), the phasing of the moons is approximately equal to the desired phasing depicted in Figure 3.

A special case in the solution space occurs when the the moons are in orbital resonance with one another, for example Io, Europa, and Ganymede that are in a 1:2:4 Laplace Resonance. The mean motions of the moon's are expressed as [9]

$$\begin{aligned} n_I - 2n_E &= \nu \\ n_E - 2n_G &= \nu \end{aligned} \tag{50}$$

where the subscripts I, E, and G indicate the mean motions Io, Europa, and Ganymede, respectively, and ν is a small positive value. Setting these equations equal to each other gives the resonance condition $n_I - 3n_E + 2n_G = 0$. Then $n_E = \frac{n_I - \nu}{2}$, $n_G = \frac{n_E - \nu}{2}$. The synodic periods are expressed as

$$\begin{aligned} Ts_{EI} &= \frac{2\pi}{n_E + \nu} = \frac{4\pi}{n_I + \nu} \\ Ts_{GE} &= \frac{2\pi}{n_G + \nu} = \frac{4\pi}{n_E + \nu} \\ Ts_{GI} &= \frac{2\pi}{3(n_G + \nu)} = \frac{8\pi}{3(n_I + \nu)} \end{aligned} \tag{51}$$

In each case, if $\nu = 0$ then the absolute phasing of the first flyby moon will return to the same value after an integer multiple of synodic periods. For example, if the first flyby body is Ganymede and the second is Io then Ganymede will return to the same location after three synodic periods. More

Table 1: Drift and drift rates from a repeating pattern

Sequ.	Syn. Per. (days)	Drift (rad/syn. per.)	Total Drift/cycle (deg.)
G-I	2.35	$-\frac{2\pi}{3}\frac{\nu}{n_G}$	-5.3
G-E	7.05	$-2\pi\frac{\nu}{n_G}$	-5.3
E-G	7.05	$-4\pi\frac{\nu}{n_E}$	-5.3
E-I	3.53	$-2\pi\frac{\nu}{n_E}$	-2.6
I-G	2.35	$-\frac{8\pi}{3}\frac{\nu}{n_I}$	-5.2
I-E	3.53	$-4\pi\frac{\nu}{n_I}$	-2.6

All combinations have a drift rate of -ν.

Table 2: Drift and drift rates of the Callisto combinations

Sequ.	Synodic Period (days)	Total Drift/cycle (deg.)
C-I	1.98	42.7
I-C	1.98	402.7(42.7)
C-E	4.51	97.3
E-C	4.51	457.3(97.3)
C-G	12.52	270.1
G-C	12.52	630.1(270.1)

accurately,

$$\theta_{1,1}(m) = \theta_{1,1}(0) + m\left(\frac{2\pi}{3}\right)\left(\frac{1}{1+\frac{\nu}{n_G}}\right) \approx \theta_{1,1}(0) + m\left(\frac{2\pi}{3}\right)\left(1-\frac{\nu}{n_G}\right) \tag{52}$$

and Ganymede drifts from its original location by approximately $2\pi\frac{\nu}{n_G}$ every three synodic periods. Table 1 shows the first order drift rates for each combination. Using $\nu = 0.74$ deg/day [10] and $|\Delta t| < 40$ days results in a drift of nearly ±30 deg. Therefore, if the proper phasing lies just outside of the heuristic range then the maximum time until the next opportunity is 405 days. However, it is unlikely that an equivalent interplanetary trajectory will exist at this time. Callisto is not in the Laplace resonance with the other moons. Generally for any combination m$_1$-m$_2$ the synodic period is $2\pi\frac{n_1}{|n_2-n_1|}$ with a drift rate of n_1, see Tab. 2.

4. Integrated Trajectories

4.1. NLP Cleanup

Trajectories that satisfy the phasing criteria may be transitioned into high-fidelity solutions. The circular, coplanar assumption of the moons employed the preceding analytical approaches are generally accurate for estimating performance, however they introduce non-trivial degradation when immediately applied as a high-fidelity initial guess. Therefore, a fast and robust pre-conditioning step is added that removes assumptions #1 and #3 from the process outlined in Section 2 and introduces moon ephemerides to the modeling, necessitating three-dimensional spacecraft motion. The FMF process is summarized here, but the FFM procedure is fundamentally very similar.

For the FMF problem in the ephemeris, the first moon B-plane aim point ($B_{\theta 1}$) and JOI must contribute targeting the second moon as well as energy reduction. Any non-tangential targeting contribution from the JOI reduces the efficiency of the maneuver, however since the solutions satisfy phasing within the prescribed tolerance, the efficiency loss is expected to be small. Additionally, the targeting contribution in $B_{\theta 1}$ may lead to inefficiency in energy reduction. Optimization of the JOI maneuver is thus a function of the moon encounter times, t_1 and t_2, $B_{\theta 1}$ and the perijove time t_p and position $\mathbf{r}_p$ where JOI occurs. Since t_1 and t_2 specify the ephemeris state vector of each moon, t_p is a free variable, the capture sequence is fully defined by solving two fully specified, independent zero-revolution Lambert problems, namely

$$\begin{aligned} \left\{\mathbf{v}_1^+, \mathbf{v}_p^-\right\} &= \mathbf{f}\left(t_p - t_1, \mathbf{r}_1(t_1), \mathbf{r}_p\right) && (53) \\ \left\{\mathbf{v}_p^+, \mathbf{v}_2^-\right\} &= \mathbf{f}\left(t_2 - t_p, \mathbf{r}_p, \mathbf{r}_2(t_2)\right) && (54) \end{aligned}$$

Equations (53)-(54) can be solved with well-known approaches such as the Gooding algorithm.[11] With the Lambert trajectories solved, $\mathbf{v}_{\infty 1}^+$ and $\mathbf{v}_{\infty 2}^-$ are immediately available via Eq. (31) and Eq. (32), respectively. In addition, the JOI is available from the $\Delta\mathbf{v}$ due to the velocity discontinuity between the two independent arcs, i.e.,

$$\Delta v = ||\mathbf{v_p}^+ - \mathbf{v_p}^-|| \tag{55}$$

A feasible dual capture must still satisfy equality constraints on the fixed Jovian $\mathbf{v}_\infty^-$ vector given in Eq. (1) immediately before the first moon flyby, and a constraint on the desired Jovian capture period, T (or energy E), after the second moon flyby. Formally, the optimization problem is posed as

$$\text{Min. } J = \Delta v \tag{56}$$

Subject to

$$\mathbf{F}(\mathbf{X}) = \left\{ \begin{array}{c} v_{\infty,\text{des}} - v_\infty \\ \alpha_{e,\text{des}} - \alpha_e \\ \delta_{e,\text{des}} - \delta_e \\ E_\text{des} - E \end{array} \right\} = \mathbf{0} \tag{57}$$

where

$$\mathbf{X} = [t_1, t_2, B_{\theta 1}, t_p, \mathbf{r}_p]^T \tag{58}$$

Evaluation of Eq. (57) requires a mapping of $\mathbf{v}_{\infty 1}^- = \mathbf{v}_{\infty 1}^-\left(\mathbf{v}_{\infty 1}^+, B_{\theta 1}, r_{p1}\right)$ and $\mathbf{v}_{\infty 2}^+ = \mathbf{v}_{\infty 2}^+\left(\mathbf{v}_{\infty 2}^-, B_{\theta 2}, r_{p2}\right)$ where r_{p1} and r_{p2} are fixed moon flyby radii that are chosen in the phase free analysis, and $B_{\theta 2}$ is always chosen as $\beta = 0$ (maximum energy reduction) as defined in the Appendix.

These relationships may be computed through standard B-plane mapping assuming the zero sphere of influence.[12] Equation (30) yields $\mathbf{v}_1^-$, and subsequently a reference Jovian state vector $\left\{\mathbf{r}_1, \mathbf{v}_1^-\right\}$ along the incoming asymptote to the system. This state vector may be converted to standard orbital elements, and then Eq. (1) and Eqs.(6)-(9) can be used to obtain v_∞, α_e, and δ_e. Equation (33) yields $\mathbf{v}_2^+$, and subsequently, the Jovian capture orbit reference state $\left\{\mathbf{r}_2, \mathbf{v}_2^+\right\}$ that specifies E from vis-viva. The preceding optimization problem may be solved with with standard nonlinear programming (NLP) packages such as SNOPT.

The FFM problem utilizes a similar approach, but only one Lambert arc is required between the flybys. The standard B-plane mappings are used to compute $\left\{\mathbf{r}_1, \mathbf{v}_1^-\right\}$ and $\left\{\mathbf{r}_2, \mathbf{v}_2^+\right\}$ using the same assumptions. However, the moon 2 to JOI arc is analytically propagated to perijove and the JOI Δv is explicitly calculated from vis viva given E_{des}. The problem reduces to an iterative search for a unique solution of $\mathbf{X} = [t_1, t_2, B_{\theta 1}]^T$ that satisfies the first three constraints in Eq. (57).

All initial guesses satisfying the phasing criteria rapidly converge in both cases, even with numerical partial derivatives. The converged solutions are sufficiently accurate as an initial guess for the higher fidelity model.

4.2. High-Fidelity Optimization

Solutions that are solved in the NLP cleanup stage are suitable to initiate a high-fidelity, doubly-aided satellite capture design. The motion of the spacecraft in a numerically-integrated, high-fidelity model is described by a system of second order ODE's dominated by central-body gravitational acceleration

$$\ddot{\mathbf{r}} + \mu \frac{\mathbf{r}}{r^3} = \mathbf{a}_p, \tag{59}$$

where the radius $r = ||\mathbf{r}||$ is the magnitude of the inertial position vector $\mathbf{r}$. The remaining terms $\mathbf{a}_p$ are perturbing accelerations. It is noted that when $||\mathbf{a}_p|| = 0$, the fundamental system reverts to the two-body problem, and when coupled with the assumptions of the preliminary design process, reflects a model that exactly captures a solution of the doubly-aided capture problem thus far. To minimize round-off errors, the central body chosen to represent the left-hand side of Eq. (59) is always switched to the dominant gravity field as needed based on the sphere-of-influence. In general, the perturbing acceleration can capture any additional dynamical effects, but for the problem of interest it can be decomposed as

$$\mathbf{a}_p = \mathbf{a}_n + \mathbf{a}_q + \mathbf{a}_{srp} + \mathbf{a}_d + \mathbf{a}_{gr} \tag{60}$$

to reflect contributions from non-spherical gravity $\mathbf{a}_n$, third-body perturbations $\mathbf{a}_q$, solar radiation pressure $\mathbf{a}_{srp}$, atmospheric drag $\mathbf{a}_d$, and general relativity $\mathbf{a}_{gr}$. Evaluation of $\mathbf{a}_q$ requires an ephemeris file that specifies the position and velocity of all moons and planetary objects as a function of time, e.g., the Jet Propulsion Laboratory (JPL) binary ephemeris files DE430 (planets) and JUP230 (Jovian moons). For brevity, detailed discussion of the models for the perturbing accelerations is omitted, and can by found in references such as Vallado.[13] Typically, $\mathbf{a}_n$ and $\mathbf{a}_q$ will dominate the perturbations from an order-of-magnitude perspective and thus, for this analysis all other components of $\mathbf{a}_p$ are ignored.

To transition solutions into the high-fidelity integrated model described by Eq. (59), a constraint/ variable formulation is assumed that is consistent with the solution methodologies of software packages such as the Computer Optimization System for Multiple Independent Courses (COSMIC), the Computer Algorithm for Trajectory Optimization (CATO),[14] and Copernicus,[15] and adaptable to others.[16] For this analysis, the authors chose COSMIC, a package within JPL's Mission-design and Operations Navigation Toolkit Environment (MONTE) that facilitates configuration control in modeling and physical constants among mission designers on the Europa project. Free variables in the form of control points (CPs) are specified at the gravity assist bodies as well as at points where the trajectory must depart the interplanetary solution and arrive at the capture orbit. The control points are numerically integrated in forward- and reverse-time, and a break point (BP) exists where at the midpoint of two arcs. The break points are associated with discontinuities in position and velocity that must be eliminated within a prescribed tolerance. Maneuvers are also placed at control points as needed. Let any trajectory sequence consisting of a break point between a pair of control points be defined as a "leg". The goal of the high-fidelity trajectory design process is to adjust the control points and maneuvers to satisfy the BP discontinuity on each leg and minimize total Δv. With this transcription in mind, the initial high-fidelity design process is formulated as a four-leg problem, with five control points and two maneuvers. These variables, along with their rationale, are summarized in Tab. 3 and sketched in Fig. 5 for the FMF case. It is noted that CP#4 is reversed with CP #3/Mvr. #2 in Tab. 3 and Fig. 5 for the FFM scenario.

Table 3: Control variable details, FMF case

Maneuver (Mvr.) #	CP #	Leg #	Central Body	Location	Parameterization	Components to Vary wrt Central Body	# Control Variables	Rationale
-	1	1	Sun	Deep space, ∼ 1 year before capture	Cartesian	None	0	Interplanetary trajectory anchor state
1	-	1	Sun	At CP #1	Cartesian	$\Delta\mathbf{v}$	3	Flyby targeting TCM
-	2	1–2	Moon #1	Moon #1 periapsis	Hyperbolic	B_θ, $\mathbf{v}_\infty^-$, t	5	Fixed-altitude flyby state
-	3	2–3	Planet	Planetary periapsis	Hyperbolic	B_θ, $\mathbf{v}_\infty^-$, t	5	Periapsis anchor point
2	-	3	Planet	At CP #3	Spherical	$\Delta\mathbf{v}$	3	Energy reduction maneuver at periapsis
-	4	3–4	Moon #2	Moon #2 periapsis	Hyperbolic	B_θ, $\mathbf{v}_\infty^-$, t	5	Fixed-altitude flyby state
-	5	4	Planet	Post-Moon #2 planetary apoapsis	Keplerian	r_p, i, Ω, ω, t	5	Fixed-period post-capture apoapsis state

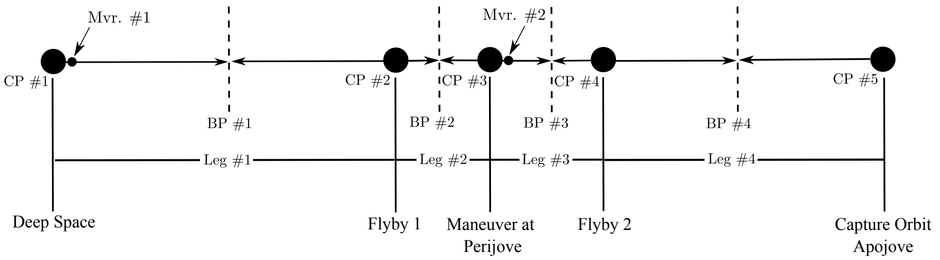

Figure 5: Control point transcription, flyby-JOI-flyby case (not to scale)

Due to the assumption that the incoming asymptote is approximately inertially fixed over the interval Δt, all components of the Trajectory Correction Maneuver (TCM), i.e. maneuver #1, are initialized to be zero. The NLP solver adjusts the TCM to account for the new time of the system entry. Once an optimal solution is found, a follow-on end-to-end high-fidelity optimization stage may be appended to actively include the preceding Earth launch sequence and any gravity assists from the interplanetary trajectory. This follow-on process is useful for reducing/eliminating the TCM and producing an end-to-end optimal total Δv that includes the launch injection maneuver and any nominal TCM's in the reference interplanetary sequence.

5. Results

Recall that the design process outlined in Fig. 2 begins with an interplanetary asymptote consistent with an enabling interplanetary trajectory. To demonstrate a detailed application of the design process, we choose an interplanetary trajectory consistent with the Europa Mission. These trajectories, along with details on the entire mission design, are summarized in detail by Lam, Camacho, and Buffington.[17] The interplanetary trajectories for the Europa mission are chosen on the basis of delivered mass requirements and the interplanetary time of flight. Currently, the mission is compatible with launch on Evolved Expendable Launch Vehicle (EELV) class (Atlas V 551, Delta IV Heavy, and Falcon Heavy) launch vehicles as well as the Space Launch System (SLS). To accomplish this cross-compatibility in terms of delivered masses to Jupiter, the EELV's require either a Venus-Earth-Earth gravity assist (VEEGA) trajectory or a Earth-Venus-Earth-Earth gravity assist (EVEEGA) trajectory, whereas the SLS launch vehicle can go direct (Earth to Jupiter). For this analysis, we analyze the 2022 interplanetary trajectory options in detail. The direct option, the 14F8 trajectory, is selected for the majority of the trade studies, while the EVEEGA option, the 15F9 [18] trajectory is used to demonstrate application of the method to a multi gravity-assist solution. A summary of the two options appears in Tab. 4 and Fig. 6.

Table 4: Interplanetary trajectory options for the Europa Mission with launch in 2022

Case	14F8	15F9
Launch Vehicle	SLS	EELV
Launch Period	Jun. 4 - 24	May 25 - Jun. 4
Trajectory Type	Direct	EVEEGA
Flight Time to Jupiter	2.1 yrs.	7.6 yrs.
Launch Δv (C3)†	6,462 m/s (81.8 $\mathrm{km}^2/\mathrm{s}^2$)	3,736 m/s (11.5 $\mathrm{km}^2/\mathrm{s}^2$)
Deep Space Maneuvers	174 m/s	6 m/s
Jupiter $v_\infty^-, \alpha_e, \delta_e$ ‡	5.718 km/s, $347.58°, -8.653°$	5.550 km/s, $4.8458°, 2.577°$
JOI Maneuver*	893 m/s	843 m/s
JOI r_p	12.0 Rj	12.1 Rj
Total Launch to JOI Δv	7,529 m/s	4,585 m/s
Jupiter Capture Orbit Period	200 days	200 days

All maneuvers are worst-case values over the entire launch period.

†200 km Earth parking orbit

‡EME2000 coordinates

*500 km Ganymede-aided capture

Given the 14F8 arrival asymptote, a database of analytical phase-free solutions is rapidly generated for all possible moon combinations. The phasing check is then applied to prune accessible moon combinations, which are summarized in Fig. 7. Through iterative application of the design process, it was found that 40 days of variation in Δt constitutes a reasonable range for this application. Recall that since the encounter moon order constrains the solution space for FFM sequences, the upper corner of Fig. 7(b) is always inaccessible due to geometry. All of the remaining solutions presented assume that the first flyby altitude is 500 km.

5.1. Flyby-Maneuver-Flyby

For the FMF cases, the six accessible combinations determined in Fig. 7(a) are selected for transition into high-fidelity solutions. Given a flyby altitude of 500 km for the second flyby, all solutions of interest are represented in Fig. 8. For reference, all 12 phase-free solutions are displayed,

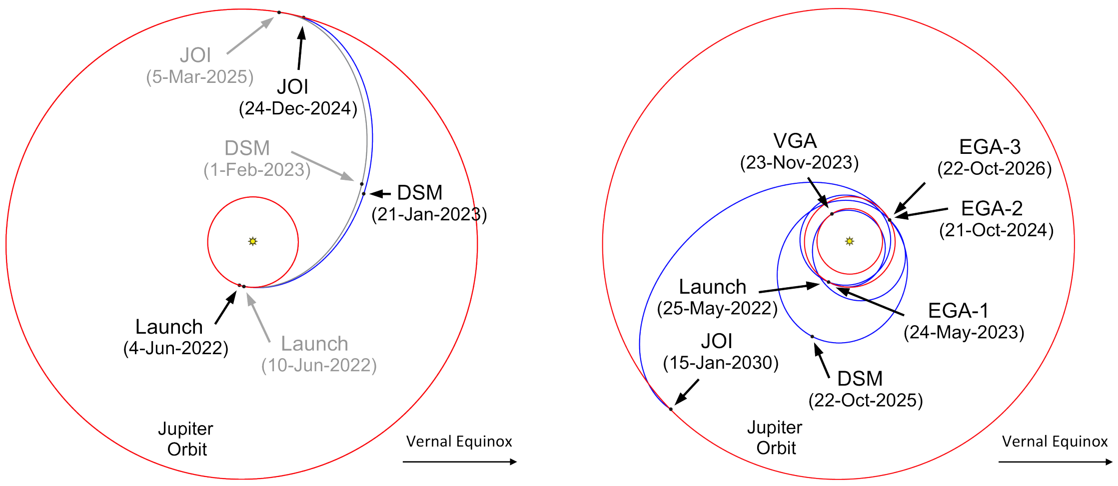

(a) 14F8 (a two-arrival-date strategy is implemented to minimize total Δv over a 21-day launch period)

(b) 15F9

Figure 6: Europa Mission interplanetary trajectories with launch in 2022 [17]

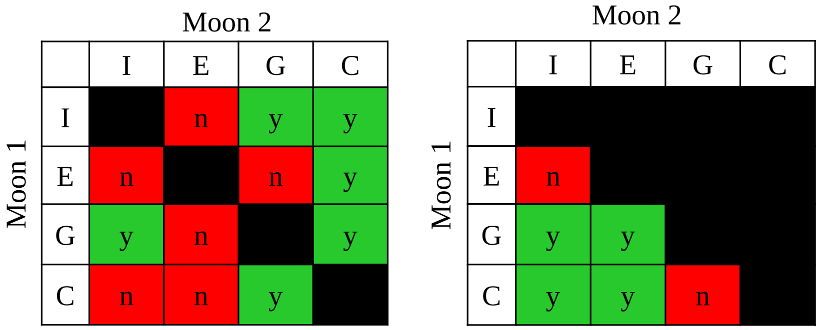

	I	E	G	C
I	■	n	y	y
E	n	■	n	y
G	y	n	■	y
C	n	n	y	■

(a) Flyby-Maneuver-Flyby

	I	E	G	C
I	■	■	■	■
E	n	■	■	■
G	y	y	■	■
C	y	y	n	■

(b) Flyby-Flyby-Maneuver

Figure 7: Phasing satisfaction of the 14F8 asymptote assuming $\Delta t < 40$ days

although those with infeasible phasing utilize thinner lines. The remaining 6 accessible solutions are represented by thicker lines. The analytical solutions in Fig. 8 yield rapid insight into the potential mission design performance. For example, Callisto-Ganymede combinations could be used to reduce the capture period to within 71 days with the same JOI as the baseline direct solution in Tab. 4. Alternatively, for the same capture period, the JOI could be reduced by 313 m/s to a value of 580 m/s.

For proof-of-concept, the six accessible combinations are discretized into a set of initial high-fidelity guesses. Following the prescribed design process, all of these guesses initially converge in the NLP cleanup, and then in the integrated environment, and are represented by the blue points in Fig. 8. For preliminary comparison, the deep space maneuvers are omitted and only the JOI values are compared. For all of the six accessible phasing combinations, the converged v_∞ in the integrated environment is re-run through the phase-free analysis in Fig. 8 to compare the JOI accuracy. In five of the six cases, the converged solutions closely match the phase-free solutions within 10 m/s.

Significant deviations in the JOI maneuver are only evident for the Ganymede-Callisto phase-free combination, which results from $\varepsilon = 17°$, the maximum allowable value in Eq. 49. Therefore, a non-trivial portion of inefficiency is introduced into the JOI to re-target moon 2. Even in this case, the JOI still yields a notable benefit compared to the baseline solution in Tab. 4

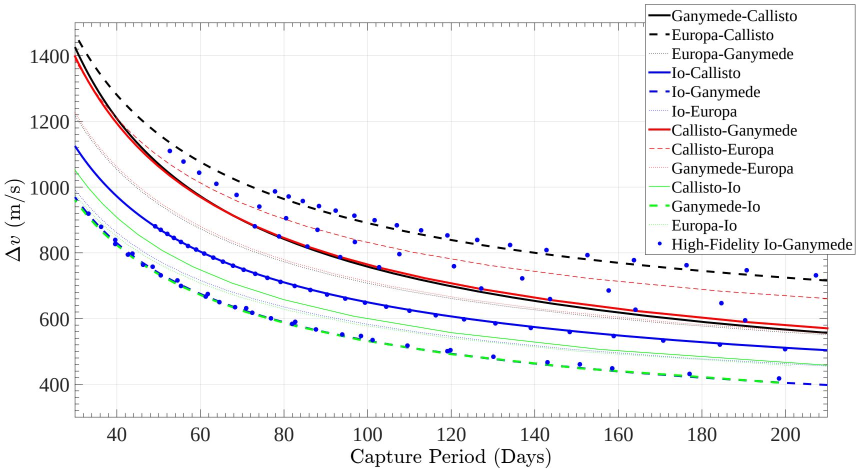

Figure 8: Phase-free versus converged, high-fidelity solutions; thinner lines indicate combinations that did not satisfy phasing constraints, altitude for second flyby is 500 km

Pragmatically any alternative option still must perform a qualitatively similar Jupiter system tour as the 14F8 trajectory. Timing, orientation, and r_p of the capture ellipse all have major impacts on achieving this goal. As an example the Callisto-JOI-Ganymede solution for a 190 day capture period is compared against the nominal solution in Tab. 5 and plotted in Fig. 9. The 4° and 2.1° differences in the capture longitude and line of apsides can be reconciled by the subsequent pump-down sequence to the first Europa flyby. This evaluation is ongoing for each of the feasible options. Since the C3 and DSM are nearly equivalent for these two options a similar delivered mass prior to JOI can be assumed. The predicted data for a starting mass of 6000 kg and an engine Isp of 300 s is plotted in Fig. 10. If the nominal period of 200 days is targeted, then nearly 500 kg of mass can be added post-JOI. For an equivalent mass, the spacecraft can be delivered into a 70 day orbit.

From a navigational perspective, a 500 km altitude for the second moon flyby may be considered too risky. Hardware uncertainties introduce state vector error in the post-JOI spacecraft state vector. In lieu of a specific altitude requirement, the capability of the FMF trajectories may also be parametrically varied by varying the altitude range up to a value of 10,000 km, which significantly reduces the effect of the flyby while reducing navigational risk. This design space is visualized in Fig. 11 using the phase-free analysis on the accessible combinations only. Here, the lines bound the expected performance envelope throughout the JOI vs. capture period trade space. Ultimately, the proper selection of flyby altitude for the second moon flyby would require a detailed navigational study.

As previously mentioned the approach is applicable to any interplanetary solution. A sample EVEEGA interplanetary trajectory with a Callisto-JOI-Europa capture sequence is shown in Fig. 12 and detailed in Tab. 6. Note that the total Δv including launch is optimized in the end-to-end trajectory.

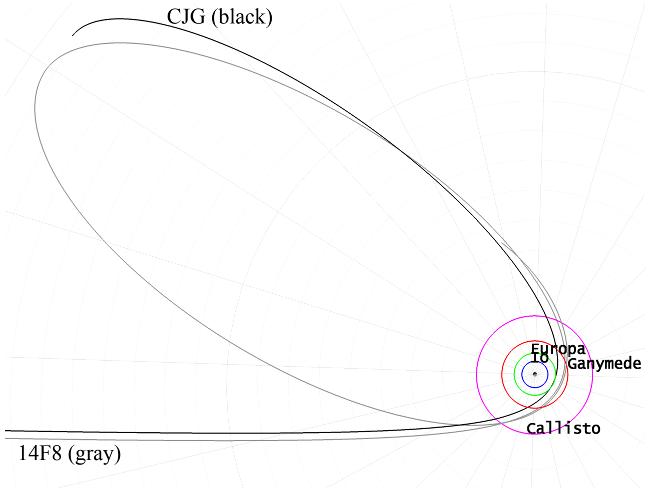

Figure 9: The nominal 14F8 and CGJ capture ellipses

Table 5: Parameters for the nominal Europa capture and the CJG point design

Parameter	14F8	CJG
Launch Date (UTC)	6/13/2022	6/13/2022
Launch C3 (km^2/s^2)	78.3	78.4
DSM Date (UTC)	3/13/2023	3/13/2023
DSM Δv (m/s)	103	104
Moon 1 Name/Alt.	G/500	C/500
Moon 1 Date	3/4/2025	3/12/2025
JOI r_p (Rj)	11.4	9.2
JOI (m/s) (Rj)	891	674
Moon 2 Name/Alt (km)	N/A	G/1,000
Moon 2 Date	N/A	3/14/2025
Capture Period (days)	198	190
Capture Long./inc. (deg.)	0.9/4.9	1.2/3.3

Angles are measured with respect an inertial frame with the z-axis aligned with the north rotational pole of Jupiter and x-y plane approximately in the plane of the moon orbits.

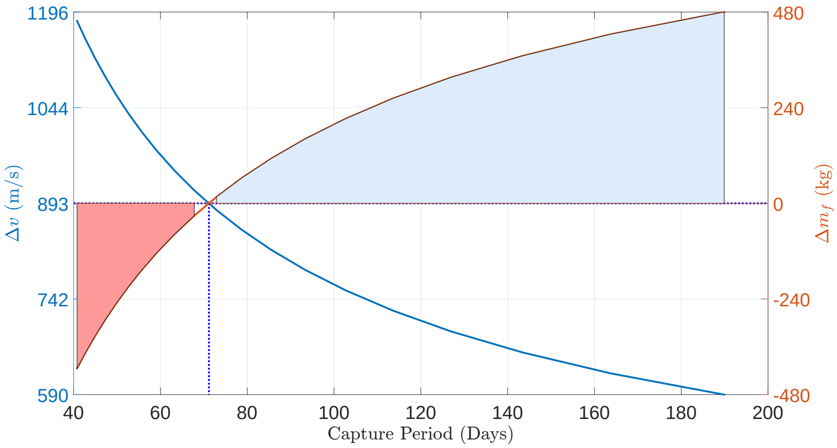

Figure 10: Mass and Δv after JOI versus capture period for the CJG case

5.2. Flyby-Flyby-Maneuver

Since the maneuver is always performed at perijove the number of combinations is significantly reduced from the FMF sequence with the feasible combinations shown in Fig. 7(b). Although a general constraint of $\Delta t < 40$ days was set for phasing, it is noted that all phasing for the FFM combinations is satisfied within $\Delta t < 20$ days, which is favorable for reducing interplanetary targeting maneuvers. Another major difference among the two cases is that for a given r_p, the JOI magnitude is pre-determined by the radius of the last node crossing for FMF solutions. Since both flybys have already been performed, the JOI for the FFM cases is a free variable.

The DSM is modified such that the incoming asymptote is expressed as: $(v_\infty^- = 5.715$ km/s $\alpha_e = 6.024^\circ,\ \delta_e = -0.106^\circ)$ in EME2000 which necessarily places the incoming hyperbola into the plane of the moons. Figure 13 shows the variation of Δv with r_p for a capture period of 200 days. The contours represent altitudes evenly spaced from 500-10,000 km for the second flyby. Returns

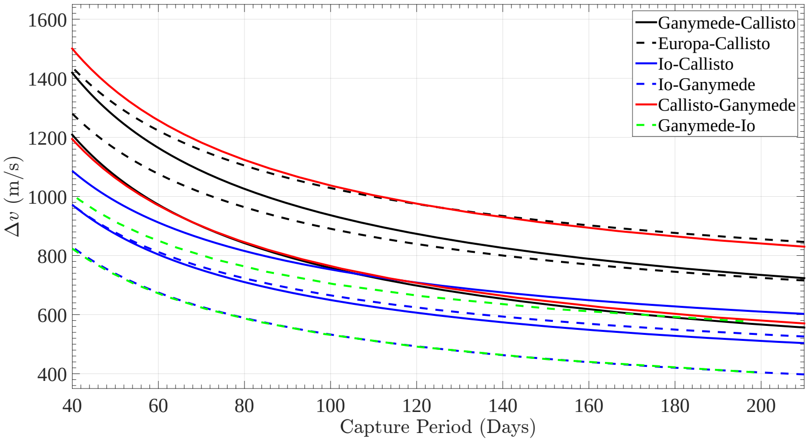

Figure 11: Upper and lower Δv bounds for the second flyby altitudes ranging from 500-10,000 km for feasible combinations

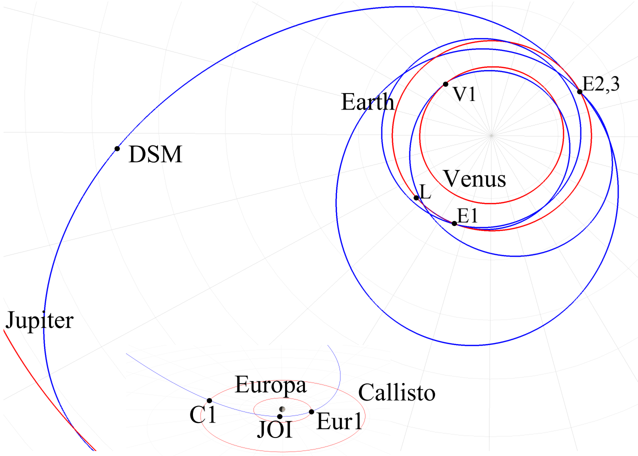

Figure 12: EVEEGA+CJE sample solution

Table 6: EVEEGA+CJE

Parameter	Value
Launch Date (UTC)	06/01/2022
Launch C3 (km^2/s^2)	10.7
DSM Date (UTC)	01/01/2028
DSM Δv (m/s)	48
Moon1 Name/Alt.	C/500
Moon1 Date	1/3/2030
JOI r_p (Rj)	6.5
JOI (m/s) (Rj)	688
Moon2 Name/Alt (km)	E/500
Moon2 Date	01/05/2030
Capture Period (days)	200

Angles are measured with respect an inertial frame with the z-axis aligned with the north rotational pole of Jupiter and x-y plane approximately in the plane of the moon orbits.

on the second flyby rapidly diminish for altitudes from 500-2,000 km. As r_p is increased towards the radius of the second flyby the Δv savings diminish as a nearly tangential approach to the second body is inefficient for energy reduction. As a point of reference, the phase-free, NLP refinement, and converged high-fidelity solutions are plotted beside each other showing close agreement. Similar agreements exist among the phase-free and converged high-fidelity solutions as in the last section.

5.3. Comparison and Launch Period Analysis

Comparison of all solutions (nominal, FMF, and FFM) is perhaps best accomplished by aggregating total Δv including the launch injection maneuver, any DSM's, and JOI. Despite specific impulse differences of individual maneuvers, this approach effectively decouples propulsion hardware from the analysis. For the detailed comparison, we compare integrated solutions within the vicinity of 14F8 in Fig. 14. All solutions are completely optimized for Δv from launch through apojove. For simplicity, the analysis is limited to trajectories with a capture period similar to the nominal solution of 200 days, and the second flyby altitude is chosen to be 500 km in order to represent a best-case

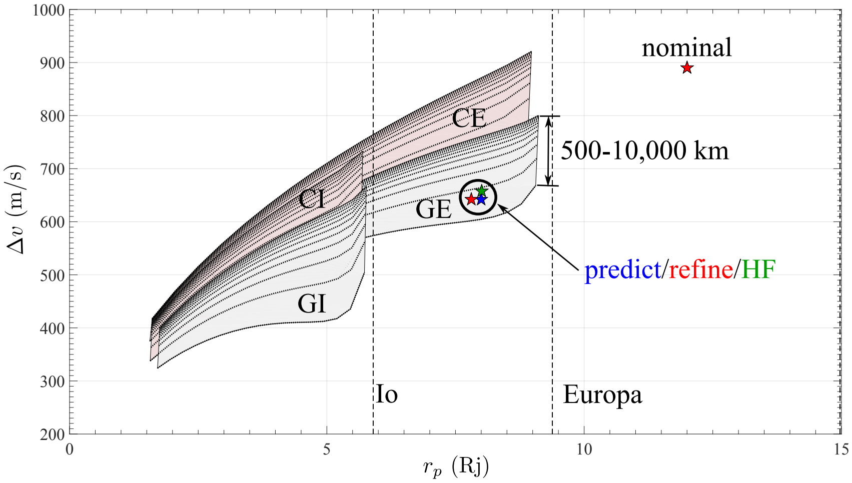

Figure 13: Sensitivity to the second flyby altitude for the FFM sequence; nominal single Ganymede flyby solution is plotted for comparison, variation in the DSM (151-172 m/s) not included.

in performance. Viewing the performance of all trajectories from this perspective is useful for weighing the potential radiation trade-offs that might further impact the system. Additionally, the perijove radii will factor into the perijove raise maneuver and any subsequent moon tour design.

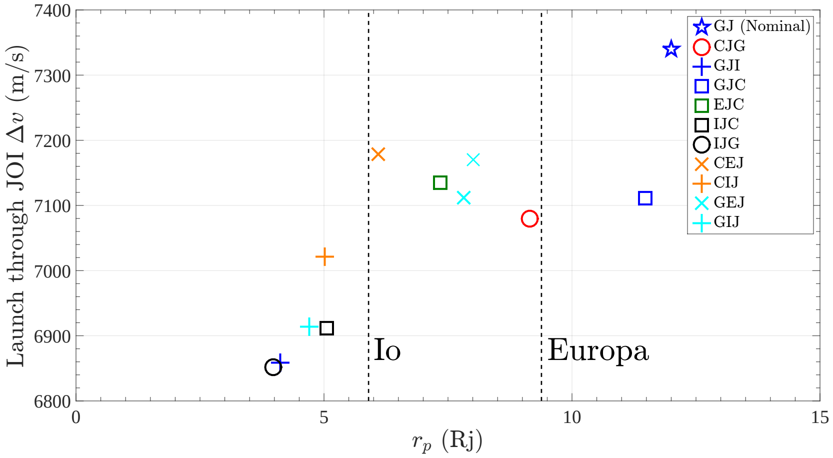

Figure 14: Launch through JOI Δv comparison of solutions in the vicinity of the nominal 14F8 arrival. All solutions have a capture period within 190-200 days, with 500 km for the second flyby altitude.

From Fig. 14 it is clear that the optimized Callisto-JOI-Ganymede (CJG) solution is highly advantageous from a Δv perspective, while maintaining a perijove radius that is very close to the nominal solution. This CJG solution is chosen for further analysis to determine, as an initial proof of concept, whether the geometry-dependent dual capture solutions might exist over the 21-day launch period that is typically expected for interplanetary missions. The launch date of this CJG solution is varied and re-optimized in the integrated environment to find an optimal envelope that bounds the performance. Considering a date range from 6/3/2022 to 6/23/2022, Fig. 15 decomposes the deterministic post-launch Δv (DSM's and JOI typically executed by the spacecraft engine) and the C3 (typically supplied by the launch vehicle upper stage) over the period. In this case, choosing two different feasible CJG arrival dates facilitates upper bounds on Δv and C3 of 807.8 m/s and 81.1 km^2/s^2, respectively. The arrival dates are spaced approximately by four months with 12/3/2024 shaded in blue and 3/12/2025 in red. The multiple arrival date strategy is enabled by the drift rate of Callisto-Ganymede (Tab. 2) which is high relative to combinations constrained to the inner three moons. The existence of the earlier arrival is also enabled by an alternate direct interplanetary trajectory with an earlier arrival date that satisfies the phasing criteria.

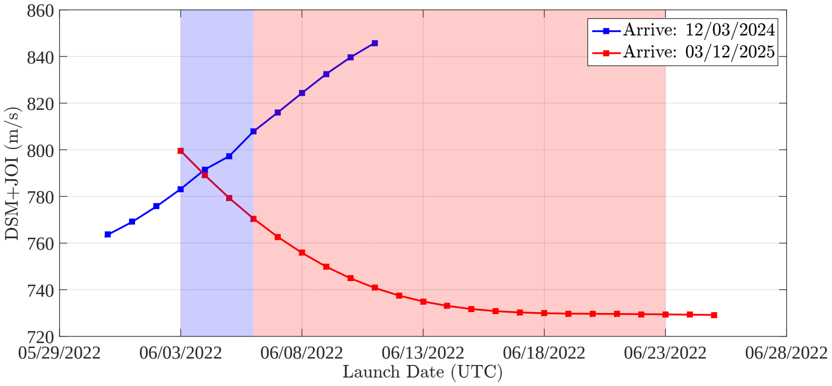

(a) DSM+JOI versus launch date

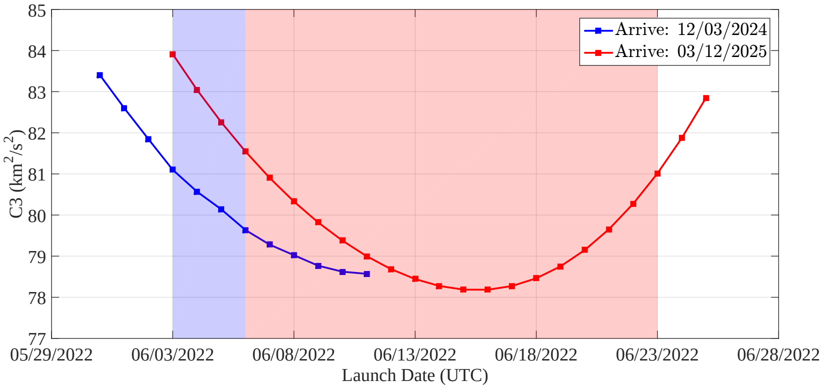

(b) C3 versus launch date

Figure 15: Conceptual CJG launch period using dual arrival dates.

6. Future Work

Future work must address many additional concerns before applicability to the Europa mission can be determined. The mission includes a tour design that specifically meets all of the broad science goals.[18] Alterations to the system entry will change the geometry of the capture ellipse, including lighting conditions, the magnitude of the periapsis raising maneuver required for subsequent flybys, and the total radiation dose. Any favorable solution must demonstrate that these changes can be compensated for without adversely impacting the achievement of these goals. Another consideration is the existence of backup launch trajectory with comparable performance to a candidate doubly aided trajectory. Additionally, a navigation analysis must prove that the spacecraft state can be estimated to an accuracy which does not place unacceptable risk to the mission.

7. Conclusions

A novel design process to robustly design doubly aided capture solutions was introduced. Key to the approach is the perspective that the qualitative aspects of the interplanetary trajectory account for the major system-driving requirements. Therefore, an assisted solution is considered a mission enhancement and the task of broadly searching for an interplanetary trajectory in order to find a favorable entry trajectory is eliminated. This process was successfully applied to the 2022 direct interplanetary trajectory for the Europa Mission using both FMF and FFM sequences, demonstrating an alternate approach to the current Ganymede-assisted baseline. Additionally, the existence of an optimized 21-day launch period for an FMF case was demonstrated by using the strategy of repeat arrival geometry. The process was further applied to the 2022 EVEEGA trajectory for the Europa Mission with an optimized, end-to-end integrated dual capture example.

Acknowledgments

The authors would like to express their gratitude to Try Lam, Jaun Arrieta Camacho, and Tom Pavlak for sharing their software expertise throughout this work. Additionally, we thank Chen-Wan Yen for her advice on modeling launch sequences. The research was in part carried out at the Jet Propulsion Laboratory, California Institute of Technology, under a contract with the National Aeronautics and Space Administration.

8. References

[1] D'Amario, L., Bright, L., and Wolf, A. "Galileo Trajectory Design." Space Science Reviews, Vol. 60, No. 1-4, pp. 23–78, 1992.

[2] Longman, R. "Gravity Assist From Jupiter's Moons for Jupiter-Orbiting Space Missions." Technical Memorandum, The RAND Corporation, RM-5479-PR, December, 1968.

[3] Longman, R. and Schneider, A. "Use of Jupiter's Moons for Gravity Assist." Journal of Spacecraft and Rockets, Vol. 7, No. 5, pp. 570–576, 1970.

[4] Cline, J. "Satellite Aided Capture." Celestial Mechanics, Vol. 19, pp. 405–415, 1979.

[5] Nock, K. and Uphoff, C. "Satellite Aided Orbit Capture." AAS/AIAA Astrodynamics Specialist Conference, Paper No. AAS 79-165, Provincetown, Massachusetts, June 25-27, 1979.

[6] Lynam, A., Kloster, K., and Longuski, J. "Multiple-satellite-aided capture trajectories at Jupiter using the Laplace resonance." Celestial Mechanics and Dynamical Astronomy, Vol. 109, pp. 59–84, 2011.

[7] Lynam, A. "Broad-Search Algorithms for the Spacecraft Trajectory Design of Callisto-Ganymede-Io Triple Flyby Sequences from 2024 to 2040, Part I: Heuristic pruning of the search space." Acta Astronautica, Vol. 94, pp. 246–252, 2014.

[8] Lynam, A. "Broad-search Algorithms for the Spacecraft Trajectory Design of Callisto-Ganymede-Io Triple Flyby Sequences from 2024 to 2040, Part II: Lambert Pathfinding and Trajectory Solutions." Acta Astronautica, Vol. 94, pp. 253–261, 2014.

[9] Greenberg, R. "Galilean Satellites: Evolutionary Paths in Deep Resonance." Icarus, Vol. 70, pp. 334–347, 1987.

[10] Showman, A. and Malhotra, R. "Tidal Evolution into the Laplace Resonance and the Resurfacing of Ganymede." Icarus, Vol. 127, pp. 93–111, 1997.

[11] Gooding, R. "A Procedure for the Solution of Lambert's Orbital Boundary-Value Problem." Celestial Mechanics and Dynamical Astronomy, Vol. 48, pp. 145–165, 1990.

[12] Sergeyevsky, A., Snyder, G., and Cunniff, R. "Interplanetary Mission Design Handbook, Volume 1, Part 2: Earth to Mars Ballistic Mission Opportunities, 1990-2005." JPL Publication 82-43, NASA Jet Propulsion Laboratory, September 15, 1983, pp. 18-24.

[13] Vallado, D. Fundamentals of Astrodynamics and Applications, Third Edition. Microcosm Press, Hawthorne, California, 2007.

[14] Byrnes, D. and Bright, L. "Design of High Accuracy, Multiple Flyby Trajectories Using Constrained Optimization." AAS/AIAA Astrodynamics Specialist Conference, Paper No. AAS 95-307, Halifax, Nova Scotia, Canada, August 14-17, 1995.

[15] Ocampo, C., Senent, J., and Williams, J. "Theoretical Foundation of Copernicus: A Unified System for Trajectory Design and Optimization." Technical Memorandum, NASA Technical Reports Server, Document ID: 20100017708; Report Number: JSC-CN-20552, May 21, 2010.

[16] Atchison, J., Ozimek, M., Scott, C., and Siddique, F. "Robust High-Fidelity Gravity-Assist Trajectory Generation Using Forward/Bckward Multiple Shooting." 25th AAS/AIAA Space Flight Mechanics Meeting, Paper No. AAS 15-249, Williamsburg, Virginia, January 11-15, 2015.

[17] Lam, T., Camacho, J. A., and Buffington, B. "The Europa Mission: Multiple Europa Flyby Trajectory Design Trades and Challenges." AAS/AIAA Astrodynamics Specialist Conference, Paper No. AAS 15-657, Vail, Colorado, August 9-13, 2015.

[18] Buffington, B. "Trajectory Design for the Europa Clipper Mission Concept." AIAA/AAS Astrodynamics Specialist Conference, Paper No. AIAA 2014-4105, San Diego, California, Auguest 4-7, 2014.

Appendix

The space of all possible post-flyby excess velocities is formed by a cone whose axis is aligned with the incoming excess velocity vector $\mathbf{v}_\infty^-$ and with a half-angle equal to the turn angle $\delta = 2\arcsin\left(\frac{1}{e_f}\right)$. Here, $e_f = 1 + \frac{r_{pf} v_\infty^2}{\mu_b}$ is the eccentricity relative to the flyby body, where r_{pf} is the periapsis radius of the flyby hyperbola, and μ_b is the gravitational mass parameter of the flyby body. The distance from the vertex to the base of the cone is v_∞, i.e., the magnitude of $\mathbf{v}_\infty^-$ and $\mathbf{v}_\infty^+$, as depicted in Fig. 16. The pump angle, α, orients the incoming excess velocity vector relative to the flyby body velocity, $\mathbf{v}_b$, as defined with respect to the central body. The pump angle is illustrated in Fig. 17, where $\mathbf{v}_c^-$ represents the pre-flyby spacecraft velocity relative to the central body. The $\hat{\mathbf{i}} - \hat{\mathbf{j}}$ plane in Fig. 16 contains the vectors $\mathbf{v}_b$ and $\mathbf{v}_c^-$, and $\hat{\mathbf{i}}$ is aligned with $\mathbf{v}_\infty^-$. The turn, pump, and B-plane angles are defined within the ranges $\delta \in [0, \pi]$, $\alpha \in [0, \pi]$, $\beta \in [0, 2\pi]$, respectively

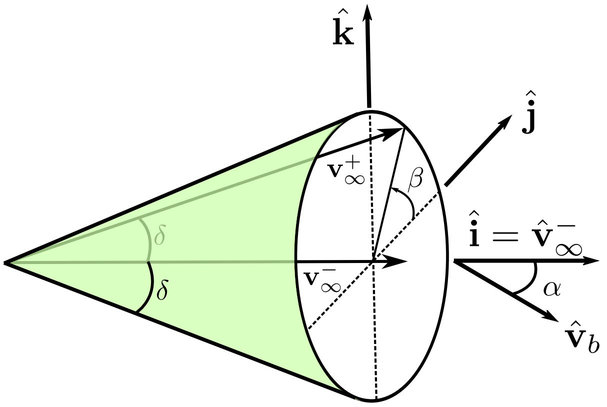

Figure 16: Geometry of possible post-flyby excess velocity orientations

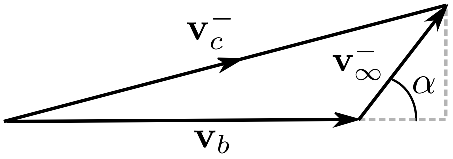

Figure 17: Pump angle geometry

The change in energy effected by the flyby can be derived and is given as

$$\Delta E = v_b v_\infty \left[\cos\alpha(\cos\delta - 1) - \sin\alpha\cos\beta\sin\delta\right] \tag{61}$$

Assuming the angle ranges given for α and δ, the second term within the brackets, $(-\sin\alpha\cos\beta\sin\delta)$, is minimized for $\beta = 0$. Thus, for given values of α and δ, the post-flyby energy is minimized via a flyby for which the B-plane angle β is zero.